Received: Added at production | Revised: Added at production | Accepted: Added at production

DOI: xxx/xxxx

RESEARCH ARTICLE

Vibration-based detection and classification of structural changes using principal component analysis and *t*-distributed stochastic neighbor embedding

David Agis[1] | Diego A. Tibaduiza[2] | Francesc Pozo*[1]

[1]Control, Modeling, Identification and Applications (CoDAlab), Department of Mathematics, Escola d'Enginyeria de Barcelona Est, Universitat Politècnica de Catalunya, Campus Diagonal-Besòs, Eduard Maristany, 16, Barcelona 08019, Spain

[2]Departamento de Ingeniería Eléctrica y Electrónica, Universidad Nacional de Colombia, Carrera 45 # 26-85, Bogotá, Colombia

Correspondence
Francesc Pozo, Control, Modeling, Identification and Applications (CoDAlab), Department of Mathematics, Escola d'Enginyeria de Barcelona Est (EEBE), Universitat Politècnica de Catalunya (UPC), Campus Diagonal-Besòs (CDB), Eduard Maristany 16, Barcelona 08019, Spain
Email: francesc.pozo@upc.edu

Summary

This paper describes a structural health monitoring strategy to detect and classify structural changes in structures that can be equipped with sensors. The proposed approach is based on the *t*-distributed stochastic neighbor embedding (*t*-SNE), a nonlinear technique that can represent the local structure of high-dimensional data collected from multiple sensors in a plane or spatial representation. We propose the following basic steps for the detection and classification. First, the raw data are preprocessed: we scale the data using the mean-centered group scaling and apply principal component analysis to reduce the dimensionality of the scaled data. Second, *t*-SNE is applied to represent the scaled and reduced data as points in a plane, defining a cluster for each structural state. Finally, the current structure to be diagnosed is associated with a cluster (or structural state) using three different strategies: (a) the smallest point-centroid distance; (b) the majority voting; and (c) the sum of the inverse distances. The combination of *t*-SNE with our preprocessing and the three proposed classification strategies significantly improves the quality of the clusters that represent different structural states. We evaluate the performance of our method using experimental data from an aluminum plate instrumented with piezoelectric transducers. Results are presented in the time domain, and they reveal the high classification accuracy and strong performance of this method, with a percentage of correct decisions close to 100% in several scenarios.

KEYWORDS:
Classification, detection, principal component analysis (PCA), structural changes, structural health monitoring (SHM), *t*-distributed stochastic neighbor embedding (*t*-SNE).

1 | INTRODUCTION

Structural health monitoring (SHM) is an essential process for engineering structures: it verifies the correct performance of the structure and determines whether it needs maintenance. The healthy state of the structure must remain between the specified limits or threshold; however, these limits may change due to the aging of the structure and its use, or due to the environmental and operational conditions (EOC). Therefore, in SHM systems, it is important to detect and classify structural changes, which helps to improve safety and reduce maintenance costs. If damage is detected and classified just as it occurs, some action may be

taken before a human and/or economic disaster occurs, thereby reducing the probability of accidents and costs of inspection and maintenance. SHM has been applied in countless structures such as buildings[1,2], wind turbines[3,4], and aircrafts[5,6]. A review of the state-of-the-art literature reveals that SHM is a very active research area.

To monitor the state of the structure, data are collected from multiple sensors. This sensor network is placed along with the structure. The signals extracted from multiple sensors are gathered in a high-dimensional dataset, which contains a large volume of data because of continuous measurements of the monitoring system. Several methods have been proposed for the management of high-dimensional, big, and complex data. Among these methods, plane or spatial representation techniques stand out, as they can help to represent data using an intuitive interface that allows people to easily detect natural clusters, identify hidden patterns, et cetera[7]. Plane or spatial representation techniques are also somehow related to dimensionality reduction. Dimensionality reduction is the process of reducing the dimension of the original data keeping the most important intrinsic information[8]. One of the previously proposed methods of dimensionality reduction is *t*-distributed stochastic neighbor embedding (*t*-SNE), a technique developed by L. van der Maaten and G. Hinton[9], which represents the local structure of original high-dimensional data in a low-dimensional space (for example, a simple scatter plot). This technique detects patterns by identifying clusters based on the similarity of data points. *t*-SNE is widely used in the literature for dimensionality reduction, classification, pattern recognition, or visualization and compression of big datasets. Although *t*-SNE has been applied in several fields, this is one of the first approaches that uses *t*-SNE in the field of SHM.

In this study, we propose an SHM strategy to detect and classify structural changes using two-step data integration (type *E* unfolding[10] and the so-called mean-centered group scaling (MCGS)), data transformation using principal component analysis (PCA), and two-step data reduction combining PCA and *t*-SNE. PCA is a common technique that is mainly used for dimensionality reduction or feature extraction in the field of pattern recognition[11]; moreover, it can also be applied to detect and classify structural changes or faults[12]. In our study, the PCA model will help to detect different types of damage, not only the *healthy* structures. In some cases, however, we observe that using only the first few principal components does not help with visual grouping, clustering, or separation. For this reason, we propose to detect damage or faults using the combination of PCA and *t*-SNE. Hence, we use the following basic steps for detection and classification: (i) first, we scale the collected data using MCGS, because of different scales and magnitudes in the measurements; (ii) then, we apply PCA to obtain a better representation of the original data; thus, we reduce the dimensionality of the scaled data and then project the scaled data into the vectorial space spanned by the principal components; and (iii) finally, we apply *t*-SNE to the projected data to represent these points in a plane. We will show that, compared with the PCA, the quality of the clusters related to different structural states is significantly improved. Specifically, the current structure to be diagnosed will then be associated with a structural state using three different strategies: (i) the smallest point-centroid distance (when a single actuation phase is considered); (ii) majority voting; and (iii) sum of the inverse distances (when several actuation phases are combined). Therefore, in this study, *t*-SNE is used (in combination with particular data integration, data transformation, and data reduction) for the first time in the field of SHM in a time-based approach. In comparison with previous strategies found in the literature, this novel method can yield the best detection and classification of structural changes, thus, leading to the best performance.

We evaluate the proposed method for the detection and classification of structural changes using experimental data from an aluminum plate instrumented with piezoelectric transducers (PZTs) attached to its surface. Because guided wave propagation-based SHM strategies have proven their ability to adequately identify defects in structures[13,14,15,16], in our study, we have also considered the paradigm of guided waves. In this paradigm, the structure is excited by a signal, and the response is measured to create a baseline pattern. When a new structure must be diagnosed, it must be excited by the same signal, and the response is measured and compared with the baseline pattern. Results show a high classification accuracy and strong performance of this method, with a percentage of correct decisions close to 100% in several scenarios. We must highlight that the environmental conditions were not considered in the present study, as it will be a topic for further developments.

The remainder of this paper is structured as follows. Section 2 describes how we collect and preprocess the baseline data, reduce the global dimension of the data, and create the clusters using *t*-SNE. The damage detection and classification procedure for a structure that must be diagnosed is presented in Section 3. The experimental case studies are described in Section 4. In Section 5, the results are shown. Finally, in Section 6, some conclusions are drawn.

2 | DATA PREPROCESSING AND CLUSTERING: BASELINE DATA

Contributions of our study include the methods of data preprocessing: how the data are collected, arranged, scaled, transformed, and reduced. In the following subsections, data preprocessing is presented in sufficient detail, so that the proposed approach can be easily reproduced. The preprocessing is divided into three stages: data integration (Section 2.1), data transformation (Section 2.2), and data reduction (Section 2.3). Figure 1 illustrates these three stages. Finally, data are organized in clusters in Section 2.4.

2.1 | Data integration

In this study, data integration is defined as combining different response signals (measured by different sources during multiple observations) into a single and unified view. In our case, this unified view will be represented by a matrix. Section 2.1.1 presents the unfolding of the raw data (measured by the sensors) that are naturally stored as a 3-dimensional matrix. Section 2.1.2 describes the standardization of these data.

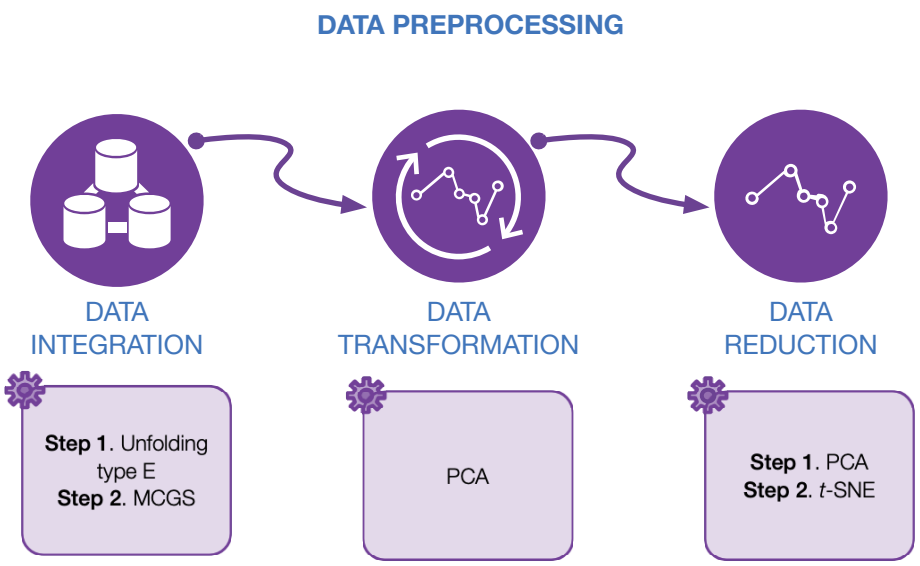

FIGURE 1 Preprocessing is divided into three stages: data integration (including unfolding and scaling), data transformation, and data reduction (PCA and *t*-SNE).

2.1.1 | Type *E* unfolding

The collected data include different response signals measured by sensors on a vibrating structure. Multiple observations of these responses are measured under different structural states. A matrix that collects all observations under different structural

states is defined as follows:

$$\mathbf{X} = \left(x_{i,l}^{k,j}\right) = \left[\begin{array}{ccc:ccc:c:ccc} x_{1,1}^{1,1} & \cdots & x_{1,1}^{1,L} & x_{1,1}^{2,1} & \cdots & x_{1,1}^{2,L} & \cdots & x_{1,1}^{N,1} & \cdots & x_{1,1}^{N,L} \\ \vdots & \ddots & \vdots & \vdots & \ddots & \vdots & \ddots & \vdots & \ddots & \vdots \\ x_{n_1,1}^{1,1} & \cdots & x_{n_1,1}^{1,L} & x_{n_1,1}^{2,1} & \cdots & x_{n_1,1}^{2,L} & \cdots & x_{n_1,1}^{N,1} & \cdots & x_{n_1,1}^{N,L} \\ \hdashline x_{1,2}^{1,1} & \cdots & x_{1,2}^{1,L} & x_{1,2}^{2,1} & \cdots & x_{1,2}^{2,L} & \cdots & x_{1,2}^{N,1} & \cdots & x_{1,2}^{N,L} \\ \vdots & \ddots & \vdots & \vdots & \ddots & \vdots & \ddots & \vdots & \ddots & \vdots \\ x_{n_2,2}^{1,1} & \cdots & x_{n_2,2}^{1,L} & x_{n_2,2}^{2,1} & \cdots & x_{n_2,2}^{2,L} & \cdots & x_{n_1,2}^{N,1} & \cdots & x_{n_2,2}^{N,L} \\ \vdots & \ddots & \vdots & \vdots & \ddots & \vdots & \ddots & \vdots & \ddots & \vdots \\ \hdashline x_{1,E}^{1,1} & \cdots & x_{1,E}^{1,L} & x_{1,E}^{2,1} & \cdots & x_{1,E}^{2,L} & \cdots & x_{1,E}^{N,1} & \cdots & x_{1,E}^{N,L} \\ \vdots & \ddots & \vdots & \vdots & \ddots & \vdots & \ddots & \vdots & \ddots & \vdots \\ x_{n_E,E}^{1,1} & \cdots & x_{n_E,E}^{1,L} & x_{n_E,E}^{2,1} & \cdots & x_{n_E,E}^{2,L} & \cdots & x_{n_E,E}^{N,1} & \cdots & x_{n_E,E}^{N,L} \end{array}\right] = \left[\begin{array}{c} \mathbf{X}_1 \\ \hdashline \mathbf{X}_2 \\ \hdashline \vdots \\ \hdashline \mathbf{X}_E \end{array}\right] \tag{1}$$

$$= \left[\, \mathbf{X}^1 \,\middle|\, \mathbf{X}^2 \,\middle|\, \cdots \,\middle|\, \mathbf{X}^N \,\right] \in \mathcal{M}_{(n_1+\cdots+n_E)\times(N\cdot L)}(\mathbb{R}), \tag{2}$$

where $N \in \mathbb{N}$ is the number of sensors and $k = 1, \ldots, N$ identifies the sensor that is measuring; $L \in \mathbb{N}$ is the number of components in each signal and $j = 1, \ldots, L$ indicates the $j-$th measurement; $E \in \mathbb{N}$ is the number of different structural states that are considered and $l = 1, \ldots, E$ represents the structural state that is been measured. Finally, $n_l,\ l = 1, \ldots, E$, is the number of observations per structural state and $i = 1, \ldots, n_l$ is the $i-$th observation related to the $l-$th structural state. Note that matrix $\mathbf{X}$ in Equation (1) is formed by E horizontal blocks, $\mathbf{X}_l,\ l = 1, \ldots, E$, where each block is related to a different structural state. Meanwhile, matrix $\mathbf{X}$ can also be viewed as formed by N vertical blocks, $\mathbf{X}^k,\ k = 1, \ldots, N$, where each block is related to a different sensor. Notably, matrix $\mathbf{X}$ in Equation (1) is a particular unfolded version of a 3-dimensional $(n_1 + \cdots + n_E) \times N \times L$ data matrix, where the first dimension is related to the multiple observations, the second dimension is related to the sensors in the sensor network, and the third dimension is time. To handle 3-dimensional matrices, several approaches have been proposed; the most widely adopted ones are based on the unfolding of these matrices. According to Westerhuis *et al.*[10], there are six alternative ways of arranging a 3-dimensional data matrix, which affect the performance of the overall strategy. In our study, out of the six possible unfolded matrices, we have considered type E in the classification proposed by Westerhuis *et al.*[10]. The choice of type E unfolding simplifies the study of the variability among samples, because we compile the information related to the sensor measurements and their variations over time.

2.1.2 | Mean-centered group scaling (MCGS)

We consider two main reasons for the scaling or standardization of the raw data in matrix $\mathbf{X}$ in Equation (1): first, to process data with different magnitudes that come from different sensors; second, to simplify the computations of the data transformation in Section 2.2 using PCA. How the raw data are scaled may severely affect the overall performance of the subsequent methods that have to be applied[17]. Some strategies consider each column vector in matrix $\mathbf{X}$ as an independent entity, and each element in the column vector is *normalized* by subtracting the mean of all the elements in the column and by dividing by the standard deviation of the same set of data. Therefore, in this case—that can be defined as *column scaling*—the mean of each column is zero and its standard deviation is one. A second strategy[17]—the so-called group scaling—considers the nature of the vertical blocks, where all measures come from the same sensor. In this case, each element in the block is normalized by subtracting the mean of all the elements in the block and by dividing by the standard deviation of the same set of data. The main drawback of this approach is that the mean of each column is no longer zero, and its standard deviation is no longer one. As a practical solution to this drawback, Pozo *et al.*[17] suggest the mean-centered version of the group scaling (MCGS), where the mean of each column is zero again; however, we cannot guarantee that the standard deviation of each column is one. Hence, in our study, we apply MCGS to matrix $\mathbf{X}$ in Equation (1) and obtain a scaled matrix $\breve{\mathbf{X}}$.

2.2 | Data transformation

In the current framework, data transformation is understood as an application of a particular mathematical function to each row of the scaled matrix $\breve{\mathbf{X}}$. Because the final goal is dimensionality reduction, the transformation that we use in our study is PCA.

Thanks to the choice of the MCGS, we can compute the variance-covariance matrix of $\breve{\mathbf{X}}$ in a compact way as

$$\mathbf{C}_{\breve{\mathbf{X}}} = \frac{1}{n-1}\breve{\mathbf{X}}^{\top}\breve{\mathbf{X}} \in \mathcal{M}_{(N\cdot L)\times(N\cdot L)}(\mathbb{R}). \tag{3}$$

The vectorial subspaces in the PCA model are defined by eigenvectors $\rho_k,\ k = 1, \dots, N \cdot L$, associated with the eigenvalues $\lambda_k,\ k = 1, \dots, N \cdot L$, ordered in decreasing order. The matrix

$$\mathbf{P} = \begin{bmatrix} \rho_1 & \rho_2 & \cdots & \rho_{N\cdot L} \end{bmatrix} \in \mathcal{M}_{(N\cdot L)\times(N\cdot L)}(\mathbb{R})$$

is the so-called PCA *model* and contains, written as columns, their corresponding eigenvectors $\rho_k,\ k = 1, \dots, N \cdot L$. These vectors are known as the principal components. Finally, the transformation is calculated as a matrix-to-matrix multiplication:

$$\mathbf{T} = \breve{\mathbf{X}}\mathbf{P} \in \mathcal{M}_{(n_1+\cdots+n_E)\times(N\cdot L)}(\mathbb{R}).$$

2.3 | Data reduction

In our study, we use two approaches to data reduction. First, we apply PCA in Section 2.3.1 to represent the scaled matrix $\breve{\mathbf{X}}$ in a new vectorial space with a reduced dimension and without a significant loss of information. Second, we apply *t*-SNE in Section 2.3.2 as a 2-dimensional representation technique. These two methods are combined to reduce the data complexity, as well as to reduce the computational time and effort.

2.3.1 | PCA

The eigenvectors of the variance-covariance matrix in Equation (3) define the PCA model. The eigenvalues define the partial variance of each principal component. When the *column scaling* is applied to matrix $\mathbf{X}$ in Equation (1)—this is not the case in our study—the trace of the variance-covariance matrix is equal to the number of columns of $\breve{\mathbf{X}}$, that is, $N \cdot L$. This means that the first $\ell \in \mathbb{N}$ principal components retain a proportion of the variance given by $(\lambda_1 + \cdots + \lambda_\ell)/(N \cdot L)$. However, when the MCGS is applied to scale the raw data in matrix $\mathbf{X}$ in Equation (1), the trace of the variance-covariance matrix $\mathbf{C}_{\breve{\mathbf{X}}}$ is no longer necessarily equal to $N \cdot L$. Therefore, the proportion of the variance directed along the first ℓ principal components is given by

$$\frac{\lambda_1 + \cdots + \lambda_\ell}{\lambda_1 + \cdots + \lambda_\ell + \cdots + \lambda_{N\cdot L}}.$$

In this study, we use PCA to reduce the dimensionality of the scaled dataset $\breve{\mathbf{X}}$ by selecting a reduced (but still significant) number $\ell < N \cdot L$ of principal components. Specifically, the number of principal components $\ell \in \mathbb{N}$ is chosen so that the proportion of the variance retained is at least 95%.

We perform the dimensionality reduction using the reduced PCA model:

$$\mathbf{P}_\ell = \begin{bmatrix} \rho_1 & \rho_2 & \cdots & \rho_\ell \end{bmatrix} \in \mathcal{M}_{(N\cdot L)\times\ell}(\mathbb{R}). \tag{4}$$

The scaled dataset $\breve{\mathbf{X}}$ is then projected into the vectorial space spanned by the first ℓ principal components through the premultiplication of $\mathbf{P}_\ell$ by $\breve{\mathbf{X}}$. Specifically,

$$\mathbf{T}_\ell = \breve{\mathbf{X}}\mathbf{P}_\ell \in \mathcal{M}_{n\times\ell}(\mathbb{R}). \tag{5}$$

P_ℓ in Equation (4) has been defined as the reduced PCA model that includes multiple observations under different structural states. Meanwhile, $\mathbf{T}_\ell$ in Equation (5) is the projection of the scaled dataset $\breve{\mathbf{X}}$ into the subspace spanned by the reduced PCA model.

2.3.2 | *t*-distributed stochastic neighbor embedding (*t*-SNE)

t-SNE is an enhanced modification of the so-called stochastic neighbor embedding (SNE)[18]. Compared with SNE, *t*-SNE is much easier to optimize. Moreover, *t*-SNE produces better plane or spatial representations of the original data, because it reduces the tendency to crowd points in the center of the distribution. The improvements of *t*-SNE over SNE can be partially explained

by the cost function that is different in two aspects: (i) t-SNE uses a symmetrized version of the SNE cost function with simpler gradients; and (ii) t-SNE uses a Student's t-distribution, instead of a Gaussian, to compute the similarity between two points in the low-dimensional space.

Given a collection of ν high-dimensional data points

$$\mathcal{X} = \{\mathbf{x}^i \in \mathbb{R}^D \mid i = 1, \dots, \nu,\ \nu, D \in \mathbb{N}\}, \tag{6}$$

the objective is to find a collection of low-dimensional map points $\mathcal{Y} = \{\mathbf{y}^i \in \mathbb{R}^d \mid i = 1, \dots, \nu,\ \nu, d \in \mathbb{N}\}$ that form a representation that preserves, as much as possible, the local structure of the original data $\mathcal{X}$. Typical values for d are 2 (*plane* representation) or 3 (*spatial* representation), where $d \ll D$.

To preserve local similarities of the original data $\mathcal{X}$, t-SNE first transforms the high-dimensional Euclidean distances between data points $\mathbf{x}^i$ and $\mathbf{x}^j$ into conditional probabilities by centering a Gaussian distribution at $\mathbf{x}^i$, computing the density of $\mathbf{x}^j$ under this Gaussian distribution, and re-normalizing:

$$p_{j|i} = \exp\left(\frac{-\|\mathbf{x}^i - \mathbf{x}^j\|_2^2}{2\sigma_i^2}\right) \Bigg/ \sum_{\substack{l=1 \\ l\neq i}}^{\nu} \exp\left(\frac{-\|\mathbf{x}^i - \mathbf{x}^l\|_2^2}{2\sigma_i^2}\right), \quad i, j = 1, \dots, \nu,\ i \neq j, \tag{7}$$

where $\|\mathbf{x}^i - \mathbf{x}^j\|_2^2 / \left(2\sigma_i^2\right)$ (scaled squared Euclidean distance or *affinity*) is the dissimilarity between data points $\mathbf{x}^i$ and $\mathbf{x}^j$. The variance of the Gaussian distribution, σ_i^2, is calculated automatically. Because only pairwise similarities between data points are of interest, t-SNE establishes $p_{i|i} = 0$. This conditional probability measures the similarity of $\mathbf{x}^j$ to $\mathbf{x}^i$. If two data points are close together, $p_{j|i}$ will be large. However, if two data points are separated, $p_{j|i}$ will be small.

Then, by symmetrizing the conditional probability in Equation (7), t-SNE defines the *pseudo*-joint probability as

$$\begin{aligned} p_{ij} &= \left(p_{j|i} + p_{i|j}\right)/(2\nu),\ i, j = 1, \dots, \nu,\ i \neq j, \\ p_{ii} &= 0. \end{aligned}$$

The *pseudo*-joint probability also measures the pairwise similarity between data points $\mathbf{x}^i$ and $\mathbf{x}^j$. Hence, we define the similarity matrix $\mathcal{P} \in \mathcal{M}_{\nu\times\nu}(\mathbb{R})$ for the high-dimensional data points as $\mathcal{P} = \left(p_{ij}\right)_{i,j=1,\dots,\nu}$.

Once the similarity matrix for the data points $\mathcal{X}$ in Equation (6) is obtained, we also define the similarity matrix $\mathcal{Q} \in \mathcal{M}_{\nu\times\nu}(\mathbb{R})$ for the map points $\mathcal{Y}$. We build matrix $\mathcal{Q}$ following the same idea as for the similarity matrix $\mathcal{P}$ regarding the original data points. The only difference is that we use, for matrix $\mathcal{Q}$, a re-normalized Student's t-distribution with one degree of freedom and $\sigma_i^2 = \frac{1}{2}$ for all i, instead of a Gaussian distribution:

$$q_{ij} = \frac{\left[1 + \|\mathbf{y}^i - \mathbf{y}^j\|_2^2\right]^{-1}}{\sum_{k=1}^{\nu}\sum_{\substack{l=1 \\ l\neq k}}^{\nu}\left[1 + \|\mathbf{y}^k - \mathbf{y}^l\|_2^2\right]^{-1}},\ i, j = 1, \dots, \nu,\ i \neq j, \tag{8}$$

$$q_{ii} = 0, \tag{9}$$

where q_{ij} represents the local structure of the data points in the low-dimensional space.

The goal is to select the map points such that the two similarity matrices, $\mathcal{P}$ and $\mathcal{Q}$, are as similar as possible. The similarity between these two matrices will be defined in terms of the Kullback–Leibler (KL) divergence. The KL divergence between the *pseudo*-joint probability distributions $\mathcal{P}$ and $\mathcal{Q}$ measures the *distance* between the two similarity matrices, and it can be defined as[9,18,19]

$$C = \mathcal{D}_{KL}(\mathcal{P}\|\mathcal{Q}) = \sum_{i=1}^{\nu}\sum_{\substack{j=1 \\ j\neq i}}^{\nu} p_{ij} \log\left(p_{ij}/q_{ij}\right). \tag{10}$$

Therefore, minimizing the KL divergence reduces the error between these two matrices. Moreover, to minimize the cost function C, the gradient descent method is used: $\partial C/\partial \mathbf{y}^i$. Gradient descent is an iterative optimization algorithm; therefore, it updates the map point $\mathbf{y}^i$ at each step.

More details can be found in the original t-SNE paper[9].

2.4 | Clustering effect

In Section 2.3.1, the dimensionality reduction has been performed using PCA. Specifically, $n = n_1 + \cdots + n_E$ observations under E different structural states (the rows of matrix $\mathbf{X}$ in Equation (1)), which may be seen as $N \cdot L-$dimensional vectors, are projected and transformed into $\ell-$dimensional vectors. This reduction of the dimension of the original data is performed with a small loss of information (less than 5%), and it is also expected that ℓ is much smaller than $N \cdot L$.

A second dimensionality reduction is applied to the projected data in matrix $\mathbf{T}_\ell$ in Equation (5) using t-SNE, as presented in Section 2.3.2. Let us define

$$\mathbf{x}^i = \mathbf{e}_i^\top \mathbf{T}_\ell = \mathbf{e}_i^\top \breve{\mathbf{X}} \mathbf{P}_\ell \in \mathbb{R}^\ell,\ i = 1, \ldots, n$$

as the $i-$th row of matrix $\mathbf{T}_\ell$ in Equation (5). Vector $\mathbf{e}_i \in \mathbb{R}^n$ is the $i-$th element of the canonical basis. Let us also define

$$\mathcal{X} = \{\mathbf{x}^i \in \mathbb{R}^\ell \mid i = 1, \ldots, n\} \tag{11}$$

as a collection of high-dimensional data points. The objective is to find a collection of 2-dimensional map points $\mathcal{Y} = \{\mathbf{y}^i \in \mathbb{R}^2 \mid i = 1, \ldots, n\}$ that represent the original set $\mathcal{X}$ with no explicit loss of information and preserving the local structure of this set. After the application of t-SNE, we expect to observe E clusters related to E different structural states. These clusters are formed by the map points $\{\mathbf{y}^1, \ldots, \mathbf{y}^{n_1}\} \subset \mathcal{Y}$, related to the *first* structural state; $\{\mathbf{y}^{n_1+1}, \ldots, \mathbf{y}^{n_1+n_2}\} \subset \mathcal{Y}$, related to the *second* structural state; and so on. Finally, $\{\mathbf{y}^{n-n_{E-1}-n_E+1}, \ldots, \mathbf{y}^{n-n_E}\} \subset \mathcal{Y}$ are related to the *penultimate* structural state, and $\{\mathbf{y}^{n-n_E+1}, \ldots, \mathbf{y}^n\} \subset \mathcal{Y}$ are related to the *last* structural state.

3 | VIBRATION-BASED DAMAGE DETECTION AND CLASSIFICATION PROCEDURE: STRUCTURE TO DIAGNOSE

In Section 2.4, we have described how the original observations under different structural states define a set of clusters on a plane. In this section, we present the vibration-based damage detection and classification procedure for a structure that must be diagnosed.

For damage detection and classification, we need a single observation of the current structure to diagnose it. The collected data include different response signals measured by the same number of sensors N and the same number of components in each signal L, as in Equation (1). When these measures are obtained, we construct a new data vector $\mathbf{z}$:

$$\mathbf{z}^\top = \left[\, z^{1,1} \ \cdots \ z^{1,L} \,\middle|\, z^{2,1} \ \cdots \ z^{2,L} \,\middle|\, \cdots \,\middle|\, z^{N,1} \ \cdots \ z^{N,L} \,\right] \in \mathbb{R}^{N \cdot L}. \tag{12}$$

3.1 | Scaling (MCGS)

Before the collected data (coming from the structure to be diagnosed) is projected into the space spanned by the ℓ principal components, we must scale the row vector $\mathbf{z}^\top$ to define a scaled row vector $\breve{\mathbf{z}}^\top$:

$$\breve{z}^{k,j} = \frac{z^{k,j} - \mu^{k,j}}{\sigma^k}, \quad k = 1, \ldots, N,\ j = 1, \ldots, L, \tag{13}$$

where $\mu^{k,j}$ is the arithmetic mean of all the elements in the $[(k-1)L + j]-$th column of matrix $\mathbf{X}$ in Equation (1)—that is, the $j-$th column of the vertical block $\mathbf{X}^k$ in Equation (2); and σ^k is the standard deviation of all the elements in the vertical block $\mathbf{X}^k$ in Equation (2) relative to the mean value μ^k (the arithmetic mean of all the elements in the vertical block $\mathbf{X}^k$ in Equation (2)).

3.2 | Projection (PCA)

The projection of the scaled row vector $\breve{\mathbf{z}}^\top \in \mathbb{R}^{N \cdot L}$ into the space spanned by the first ℓ principal components in $\mathbf{P}_\ell$ is calculated as a vector-to-matrix multiplication:

$$\mathbf{x}^{n+1} = \breve{\mathbf{z}}^\top \cdot \mathbf{P}_\ell \in \mathbb{R}^\ell.$$

Notably, the $N \cdot L-$dimensional vector, which contains the collected data (coming from the structure to be diagnosed), is now transformed into an $\ell-$dimensional vector. We add this new point to dataset $\mathcal{X}$ in Equation (11) to define a new set:

$$\mathcal{X}' = \mathcal{X} \cup \{\mathbf{x}^{n+1}\} = \{\mathbf{x}^i \in \mathbb{R}^\ell \mid i = 1, \dots, n, n+1\}. \tag{14}$$

3.3 | *t*-SNE and final classification

We apply t-SNE to the $\ell-$dimensional dataset $\mathcal{X}'$ in Equation (14) to find a collection of 2-dimensional map points $\mathcal{Y}' = \{\mathbf{y}^i \mid i = 1, \dots, n, n+1\}$ that represent the original set $\mathcal{X}$ with no explicit loss of information and preserving the local structure of this set. Moreover, we include the map point $\mathbf{y}^{n+1}$ associated with the data point $\mathbf{x}^{n+1}$. We expect to observe the same E clusters related to E different structural states. As in Section 2.4, these clusters are formed by the map points $\{\mathbf{y}^1, \dots, \mathbf{y}^{n_1}\} \subset \mathcal{Y}$ related to the *first* structural state; $\{\mathbf{y}^{n_1+1}, \dots, \mathbf{y}^{n_1+n_2}\} \subset \mathcal{Y}$ related to the *second* structural state, and so on.

For each cluster, we compute its centroid: the mean of the values of the data points in the cluster. For instance, the centroid associated with the first structural state is

$$\mathcal{Y}_1 := \frac{1}{n_1} \sum_{i=1}^{n_1} \mathbf{y}^i = \frac{\mathbf{y}^1 + \cdots + \mathbf{y}^{n_1}}{n_1} \in \mathbb{R}^2.$$

In general, the centroid associated with the $l-$th structural state, $l = 1, \dots, E$, is the point of the plane defined as

$$\mathcal{Y}_l := \frac{1}{n_l} \sum_{i=1}^{n_l} \mathbf{y}^{\left(\sum_{j=0}^{l-1} n_j\right)+i} \in \mathbb{R}^2, \; l = 1, \dots, E, \tag{15}$$

where $n_0 = 0$. Therefore, the current structure to diagnose is associated with the $l-$th structural state if

$$l = \arg \min_{l=1,\dots,E} \|\mathcal{Y}_l - \mathbf{y}^{n+1}\|_2,$$

that is, if the minimum distance between $\mathbf{y}^{n+1}$ and each centroid corresponds to the Euclidean distance between $\mathbf{y}^{n+1}$ and $\mathcal{Y}_l$. We call this approach the smallest point-centroid distance (see Figure 2).

A flowchart of the proposed approach and how it is applied is given in Figure 3.

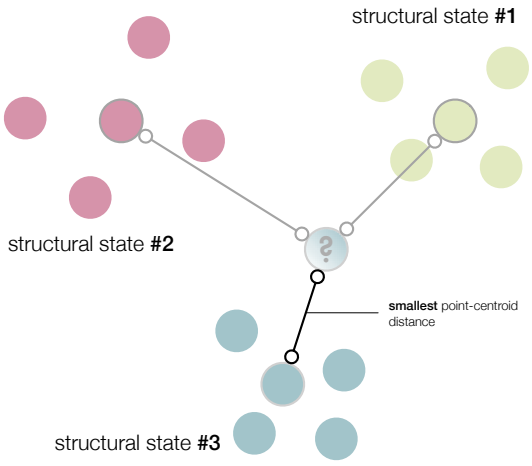

FIGURE 2 The current structure to diagnose is associated with the structural state with the smallest point-centroid distance.

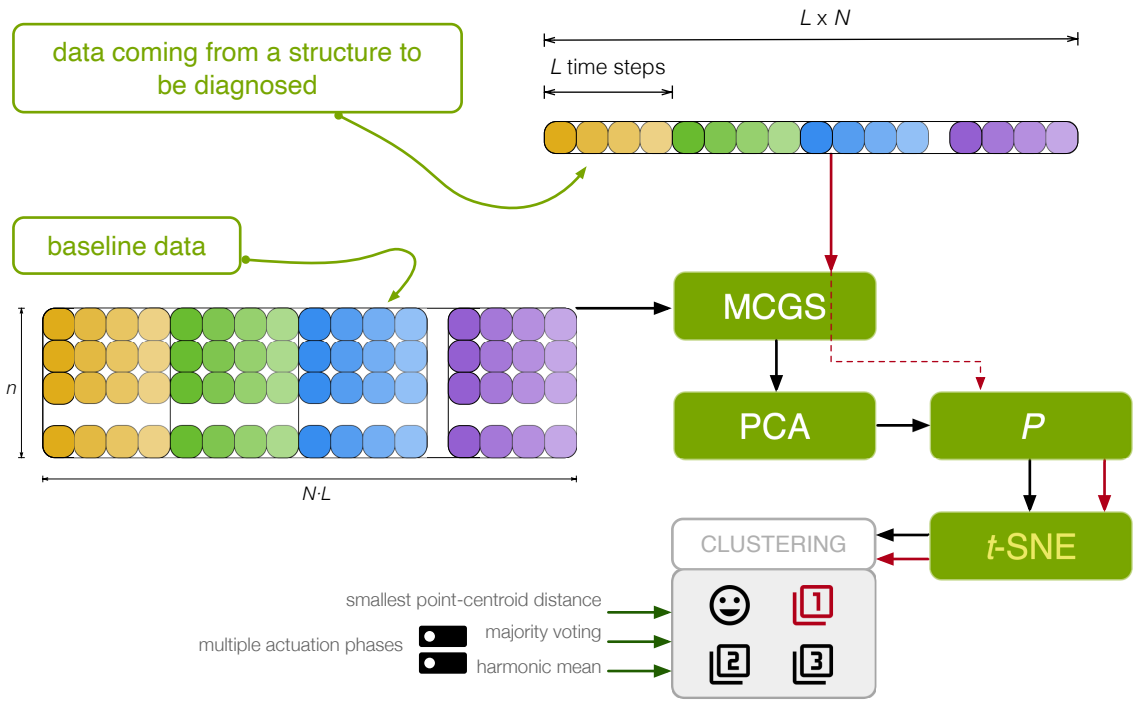

FIGURE 3 Flowchart of the proposed approach. Data coming from a structure are first scaled and then projected into the PCA model. Finally, *t*-SNE is applied to create the clusters that will be used in the vibration-based detection and classification of structural changes.

4 | CASE STUDIES: ALUMINUM PLATE WITH FOUR PZTs

4.1 | Experimental set-up

In this section, we consider a square aluminum plate with an area of 1600 cm^2 (40 cm × 40 cm, and a thickness of 0.2 cm) instrumented with four PZTs to demonstrate the reliability of the vibration-based method of damage detection and classification presented in Sections 2 and 3. The PZT discs are attached to the surface; their precise location is shown in Figure 4(a). Assuming that the origin of coordinates is placed in the lower left corner of the plate in Figure 4(a), the piezoelectric sensors are installed at these coordinates (units in centimeters):

- first PZT (S1) at $(20, 35)$;
- second PZT (S2) at $(35, 20)$;
- third PZT (S3) at $(20, 5)$; and
- fourth PZT (S4) at $(5, 20)$.

These PZTs can work both in the actuator mode (exciting the plate with the burst signal in Figure 5, thus, producing a mechanical vibration) and in the sensor mode (detecting a time-varying mechanical response). It is worth recalling that the distance between the four sensors is not the same. For example, the distance between the centers of sensor 1 and sensor 4 and the distance between the centers of sensor 1 and sensor 2 is equal ($15\sqrt{2} \approx 21.21$ cm). However, the distance between the centers of sensor 1 and sensor 3 is larger (30 cm).

We add a mass of 17.2916 grams to simulate the damage (in a non-destructive way) in the aluminum plate. This mass is a magnet attached to both sides of the plate. We use this kind of damage to change the properties of the structure (because aluminum is a non-magnetic metal) and to produce changes in the propagated wave. Thus, we obtain different scenarios for validating the proposed method. The location of the mass defines each damage. These locations are as follows (units in centimeters):

- damage 1 at $(12.5, 27.5)$;

- damage 2 at (27.5, 27.5);
- damage 3 at (12.5, 12.5).

Consequently, $E = 4$ structural states are considered here:

- the first structural state corresponds to the healthy state of the structure: the square aluminum plate with no damage;
- the second, third, and fourth structural states correspond to the plate with a mass added at the positions indicated in Figure 4(a) as damage 1, damage 2, and damage 3, respectively.

The aluminum plate is isolated from the vibration and noise in the laboratory, as shown in Figure 4(b).

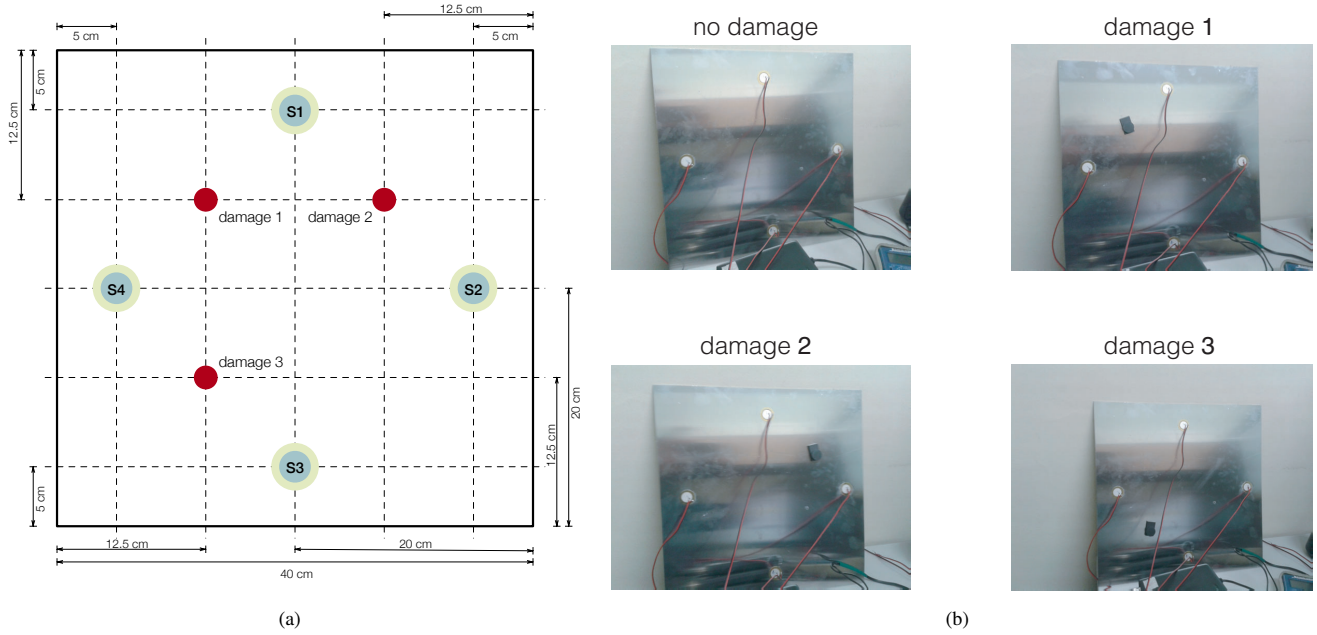

(a) (b)

FIGURE 4 (a) Aluminum plate instrumented with four piezoelectric sensors (S1, S2, S3, and S4); (b) aluminum plate with four PZTs and in four different structural states.

4.2 | Scenarios and actuation phases

The experimental setup includes three different scenarios to determine the performance of the method under the presence of white Gaussian noise, filters, and considering the length of the wire from the digitizer to the sensors:

- **Scenario 1**. The signals are acquired using a short wire (0.5 m) from the digitizer to the sensors, and these signals are filtered with a Savitzky–Golay[20] filter algorithm after adding white Gaussian noise. The filter is applied to smoothen the data.
- **Scenario 2**. The non-filtered signals are acquired using a short wire (0.5 m) from the digitizer to the sensors.
- **Scenario 3**. The signals are acquired using a long wire (2.5 m) from the digitizers to the sensors. Signals are also filtered with the Savitzky–Golay algorithm.

In this way, we can observe the effect of the following parameters on the performance of our method: using short and long wires, adding white Gaussian noise to the measured signals, and using a Savitzky–Golay filter in the detection and classification process.

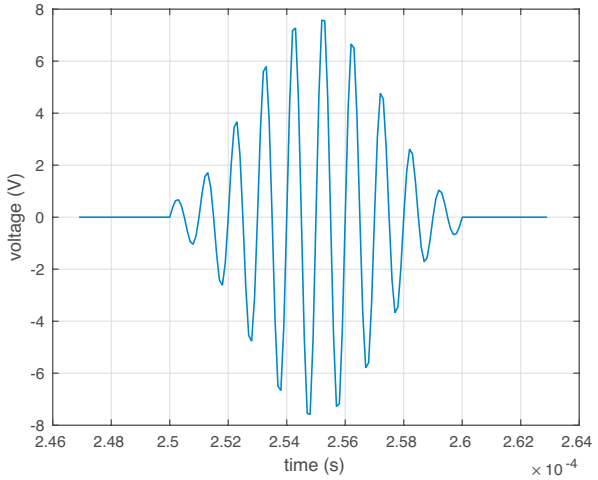

FIGURE 5 In the actuator mode, this burst signal is applied to the PZTs to produce a mechanical vibration.

As mentioned in Section 4.1, we use four PZTs (S1, S2, S3, and S4) to excite the aluminum plate and collect the measured response. This sensor network works in what we call *actuation phases*. In each actuation phase, a single PZT is used as an actuator (active sensor: the PZT excites the structure with the burst signal in Figure 5), and the rest of the PZTs are used as sensors (passive sensors: PZTs measure signals). Therefore, we have as many *actuation phases* as *sensors*:

- **Actuation phase 1**. S1 is used as the actuator. S2, S3, and S4 are used as sensors.
- **Actuation phase 2**. S2 is used as the actuator. S1, S3, and S4 are used as sensors.
- **Actuation phase 3**. S3 is used as the actuator. S1, S2, and S4 are used as sensors.
- **Actuation phase 4**. S4 is used as the actuator. S1, S2, and S3 are used as sensors.

It is very common in the literature—when using the sensor data fusion as in Vitola *et al.*[21,22]—to merge the data that come from different actuation phases in a single data matrix. In this study, we also use the approach with a single data matrix; however, we additionally examine the case where each actuation phase has a classifier, in Section 4.5.

4.3 | Actuation phases and data integration

Given a particular scenario (as the three defined in Section 4.2), we obtain four matrices $\mathbf{X}[\varphi],\ \varphi = 1, \dots, 4$ (one for each actuation phase). Each matrix $\mathbf{X}[\varphi],\ \varphi = 1, \dots, 4$, is organized as follows:

- $n_1 = n_2 = n_3 = n_4 = 25$ observations or experiments are performed for each structural state. Consequently, each matrix $\mathbf{X}[\varphi],\ \varphi = 1, \dots, 4$, consists of 100 rows (that is $n_1 + n_2 + n_3 + n_4 = 25 \cdot 4$). Specifically, the first 25 rows represent the structure with no damage, the next 25 rows are experiments where damage 1 is present in the structure, and so on.
- For each actuation phase $\varphi,\ \varphi = 1, \dots, 4$, we measure $N = 3$ PZTs working as sensors during $L = 60000$ time instants. Therefore, the number of columns of matrix $\mathbf{X}[\varphi],\ \varphi = 1, \dots, 4$, is equal to $N \cdot L = 3 \cdot 60000 = 180000$.

Therefore, the matrix that collects all observations under the four different structural states is (see Equation (1); here, $E = 4$)

$$\mathbf{X}[\varphi] = \left(x[\varphi]_{i,l}^{k,j} \right) \in \mathcal{M}_{100\times 180000}(\mathbb{R}). \tag{16}$$

The damage detection and classification procedure introduced in
Sections 2 and 3 can be applied to each matrix $\mathbf{X}[\varphi],\ \varphi = 1, \dots, 4$, in Equation (16), thereby leading to one classification per actuation phase. However, we can also use the horizontal concatenation of the four matrices $\mathbf{X}[\varphi],\ \varphi = 1, \dots, 4$, to obtain the matrix

$$\mathbf{X}[1,2,3,4] = \left[\mathbf{X}[1]\ \mathbf{X}[2]\ \mathbf{X}[3]\ \mathbf{X}[4] \right] \in \mathcal{M}_{100\times(4\cdot 180000)}(\mathbb{R}) = \mathcal{M}_{100\times 720000}(\mathbb{R}). \tag{17}$$

If matrix $\mathbf{X}[1,2,3,4]$ in Equation (17) is used for the damage detection and classification procedure introduced in

Sections 2 and 3 (this allows us to analyze the data from all actuation phases simultaneously), we obtain a single classifier that combines these four phases. Finally, we can also use the separate classifiers obtained for each actuation phase: when each actuation phase casts a vote, and the final decision is based on the four actuation phases. These strategies will be explained in Section 4.5.

4.4 | $\kappa-$fold non-exhaustive leave-p-out cross-validation

We evaluate the proposed approach by comparing *test* data (the new experiments in *unknown* state under the same conditions) with *baseline* data (data from the structure under different structural states).

For clarity, let us write $\mathbf{X}[\Phi]$ to refer to both matrix $\mathbf{X}[\varphi]$ in Equation (16) and matrix $\mathbf{X}[1,2,3,4]$ in Equation (17). Some of the rows in $\mathbf{X}[\Phi]$ will be used as the baseline data to build the model and the clusters ($\upsilon = 5$ rows per structural state), and the remaining rows are used for the validation. Specifically, we will perform five iterations ($\kappa = 5$) of a non-exhaustive leave-p-out cross-validation, where $p = \sum_{i=1}^{E} \left(n_i - \upsilon\right) = n_1 + n_2 + n_3 + n_4 - \upsilon \cdot E = 80$, to estimate the overall accuracy and avoid overfitting. For each structural state $l = 1, \dots, E$, we define permutation σ_l:

$$\begin{aligned} \sigma_l : \{1, 2, \dots, n_l\} &\to \{1, 2, \dots, n_l\}, \\ i &\to \sigma_l(i). \end{aligned}$$

In this particular case, $n_1 = n_2 = n_3 = n_4 = 25$. Therefore, in the first iteration, we use the following matrix as baseline data to build the model:

$$\mathfrak{X} = \mathbf{S}^{\top} \cdot \mathbf{X}[\Phi], \tag{18}$$

$$\mathbf{S} = \left[\mathbf{e}_{\sigma_1(1)} \ \cdots \ \mathbf{e}_{\sigma_1(5)} \middle| \mathbf{e}_{n_1+\sigma_2(1)} \ \cdots \ \mathbf{e}_{n_1+\sigma_2(5)} \middle| \cdots \middle| \mathbf{e}_{n_1+n_2+n_3+\sigma_4(1)} \ \cdots \ \mathbf{e}_{n_1+n_2+n_3+\sigma_4(5)} \right], \tag{19}$$

where $\mathbf{e}_j \in \mathbb{R}^{n_1+n_2+n_3+n_4} = \mathbb{R}^{100}$ is the $j-$th element of the canonical basis of the real vector space $\mathbb{R}^{n_1+n_2+n_3+n_4} = \mathbb{R}^{100}$ and $\mathbf{S} \in \mathcal{M}_{(n_1+n_2+n_3+n_4)\times(\upsilon \cdot E)}(\mathbb{R})$ is the *selector* matrix. Matrix $\mathfrak{X}$ in Equation (18) has been built by randomly selecting $\upsilon = 5$ rows per structural state. The $\sum_{i=1}^{E} \left(n_i - \upsilon\right) = 80$ rows of matrix $\mathbf{X}[\Phi]$ that are not used to build the model are used for the validation.

In the $i-$th iteration, $i = 1, \dots, \kappa$, we use the following matrix as baseline data to build the model:

$$\mathfrak{X} = \mathbf{S}^{\top} \cdot \mathbf{X}[\Phi], \tag{20}$$

$$\mathbf{S} = \left[\mathbf{e}_{\sigma_1(5(i-1)+1)} \ \cdots \ \mathbf{e}_{\sigma_1(5(i-1)+5)} \middle| \mathbf{e}_{n_1+\sigma_2(5(i-1)+1)} \ \cdots \ \mathbf{e}_{n_1+\sigma_2(5(i-1)+5)} \middle| \cdots \middle| \mathbf{e}_{n_1+n_2+n_3+\sigma_4(5(i-1)+1)} \ \cdots \ \mathbf{e}_{n_1+n_2+n_3+\sigma_4(5(i-1)+5)} \right], \tag{21}$$

where $\mathbf{e}_j$ is the $j-$th element of the canonical basis and $\mathbf{S}$ is the *selector* matrix. Because 80 rows of matrix $\mathbf{X}[\Phi]$ will be used for the validation step in $\kappa = 5$ iterations, the sum of all the elements in the *confusion matrices* that we will present in Section 5 is equal to $\left(\sum_{i=1}^{E} \left(n_i - \upsilon\right)\right) \cdot \kappa = 400$.

4.5 | Damage detection and classification

In this section, we present two strategies for damage detection and classification. These two strategies are as follows:

(1) the classification is based on a single matrix: $\mathbf{X}[1]$, $\mathbf{X}[2]$, $\mathbf{X}[3]$, $\mathbf{X}[4]$, or $\mathbf{X}[1,2,3,4]$, as defined in Equations (16) and (17), respectively, with $\kappa-$fold non-exhaustive leave-p-out cross-validation;

(2) the classification is based on the four matrices $\mathbf{X}[1]$, $\mathbf{X}[2]$, $\mathbf{X}[3]$, and $\mathbf{X}[4]$, defined in Equation (16), for the four actuation phases, with $\kappa-$fold non-exhaustive leave-p-out cross-validation. Each actuation phase will cast a vote to determine the final decision.

In the first strategy, we follow the next seven steps:

- **Step 1**. The data in matrix $\mathfrak{X}$ are scaled using MCGS to define a new matrix $\breve{\mathfrak{X}}$.
- **Step 2**. PCA is applied to $\breve{\mathfrak{X}}$ to obtain the PCA model $\mathbf{P}$.
- **Step 3**. The number $\ell \in \mathbb{N}$ of principal components is chosen so that the proportion of variance explained is at least 95%. Therefore, the reduced PCA model is $\mathbf{P}_{\ell}$.

- **Step 4**. A observation $\mathbf{z}^\top \in \mathbb{R}^{3\cdot 60000} = \mathbb{R}^{180000}$ (for $\mathbf{X}[1], \mathbf{X}[2], \mathbf{X}[3]$, and $\mathbf{X}[4]$) or $\mathbf{z}^\top \in \mathbb{R}^{4\cdot 180000} = \mathbb{R}^{720000}$ (for $\mathbf{X}[1,2,3,4]$) of the current structure to diagnose is needed. Then, vector $\mathbf{z}^\top$ is scaled as in Equation (13) to define $\breve{\mathbf{z}}^\top$.

- **Step 5**. Dataset $\mathcal{X}'$ is defined as $\mathcal{X}' = \{\mathbf{x}^i \in \mathbb{R}^\ell \mid i = 1, \dots, 21\}$, where

$$\mathbf{x}^i = \mathbf{e}_i^\top \breve{\mathbf{x}} \mathbf{P}_\ell, \ i = 1, \dots, 20,$$
$$\mathbf{x}^{21} = \breve{\mathbf{z}}^\top \mathbf{P}_\ell.$$

  Subsequently, t-SNE is applied to this $\ell-$dimensional dataset $\mathcal{X}'$ to find a collection of 2-dimensional map points $\mathcal{Y}' = \{\mathbf{y}^i \in \mathbb{R}^2 \mid i = 1, \dots, 21\}$.

- **Step 6**. $E = 4$ clusters are obtained and are related to the $E = 4$ different structural states. These clusters are formed by the map points: $\{\mathbf{y}^1, \dots, \mathbf{y}^5\} \subset \mathcal{Y}$, related to the *first* structural state; $\{\mathbf{y}^6, \dots, \mathbf{y}^{10}\} \subset \mathcal{Y}$, related to the *second* structural state; $\{\mathbf{y}^{11}, \dots, \mathbf{y}^{15}\}$, related to the *third* structural state; and $\{\mathbf{y}^{16}, \dots, \mathbf{y}^{20}\} \subset \mathcal{Y}$, related to the *fourth* structural state.

  Centroid $\mathcal{Y}_l, \ l = 1, \dots, E$, associated with the $l-$th structural state is computed as in Equation (15).

- **Step 7**. Finally, the current structure to diagnose is associated with the $l-$th structural state if

$$l = \arg \min_{l=1,\dots,E} \|\mathcal{Y}_l - \mathbf{y}^{21}\|_2.$$

In the second strategy, we follow **Step 1** to **Step 6** (as above) for the four matrices $\mathbf{X}[\varphi], \ \varphi = 1, \dots, 4$, related to the four actuation phases. With the information provided by the four actuation phases, we consider several approaches to finally classify the structure that must be diagnosed. One of these approaches, the majority voting, is widely used in standard fusion schemes[23], as well as *weighted majority vote* or *soft voting*. For the case studies in this work, the majority voting will be used, as well as an approach based on the sum of the inverse distances between the centroids and the map point, which is somehow related to a weighted majority vote. Here are the details of both approaches:

- **Majority voting**. In this case, the strategy of the smallest point-centroid distance is applied four times, one per the actuation phase. Therefore, four classifications are obtained for a single structure to diagnose. Specifically, each actuation phase acts as a *classifier*. Figure 6 illustrates this idea for the three actuation phases.

  The current structure to diagnose, in the $\varphi-$th actuation phase, $\varphi = 1, \dots, 4$, is associated with the $l_\varphi-$th structural state if

$$l_\varphi = \arg \min_{l=1,\dots,E} \|\mathcal{Y}_l^\varphi - \mathbf{y}_\varphi^{21}\|_2. \tag{22}$$

  It is worth remembering that $\mathbf{y}_\varphi^{21} \in \mathbb{R}^2$ is the map point associated with the observation of the current structure to diagnose. The structure is finally classified according to the most repeated classification. That is, the current structure to diagnose is associated with the $l-$th structural state if $l = \text{mode}\{l_1, l_2, l_3, l_4\}$, in the case of a unimodal set. In the case of a bimodal set, if the two modal values are l_α and l_β, the current structure to diagnose is associated with the $l-$th structural state if

$$l = \arg \min_{l \in \{l_\alpha, l_\beta\}} \sum_{\varphi=1}^{4} \|\mathcal{Y}_l^\varphi - \mathbf{y}_\varphi^{21}\|_2.$$

  Finally, if the set $\{l_1, l_2, l_3, l_4\}$ is a set with no mode, the structure is associated with the $l-$th structural state if

$$l = \arg \min_{l=1,\dots,E} \sum_{\varphi=1}^{4} \|\mathcal{Y}_l^\varphi - \mathbf{y}_\varphi^{21}\|_2.$$

- **Sum of the inverse distances**. In this case, for a given structural state, we sum the inverse of the distances between the centroids $\mathcal{Y}_l^\varphi$ and the map point $\mathbf{y}_\varphi^{21}$, for all the actuation phases $\varphi = 1, \dots, 4$. The assigned structural state is the one that obtains the highest sum. Specifically, the current structure to diagnose is associated with the $l-$th structural state if

$$l = \arg \max_{l=1,\dots,E} \sum_{\varphi=1}^{4} \frac{1}{\|\mathcal{Y}_l^\varphi - \mathbf{y}_\varphi^{21}\|_2}.$$

  Notably, the arguments of the maxima of the sum of the inverse distances is equivalent to the arguments of the minima of the harmonic mean of these distances. Figure 7 illustrates this idea for the three actuation phases. Specifically, for a given

structural state, the harmonic mean of the distances between the centroids $\mathcal{Y}_l^\varphi$ and the map point $\mathbf{y}_\varphi^{21}$ for all the actuation phases $\varphi = 1, \ldots, 4$ is

$$\frac{1}{\frac{1}{4}\sum_{\varphi=1}^{4}\frac{1}{\|\mathcal{Y}_l^\varphi - \mathbf{y}_\varphi^{21}\|_2}}.$$

Therefore,

$$l = \arg\max_{l=1,\ldots,E}\sum_{\varphi=1}^{4}\frac{1}{\|\mathcal{Y}_l^\varphi - \mathbf{y}_\varphi^{21}\|_2} = \arg\min_{l=1,\ldots,E}\frac{1}{\frac{1}{4}\sum_{\varphi=1}^{4}\frac{1}{\|\mathcal{Y}_l^\varphi - \mathbf{y}_\varphi^{21}\|_2}}.$$

Mehta *et al.*[24] also use the harmonic distance to define a pattern classification technique similar to the k-nearest neighbor classifier.

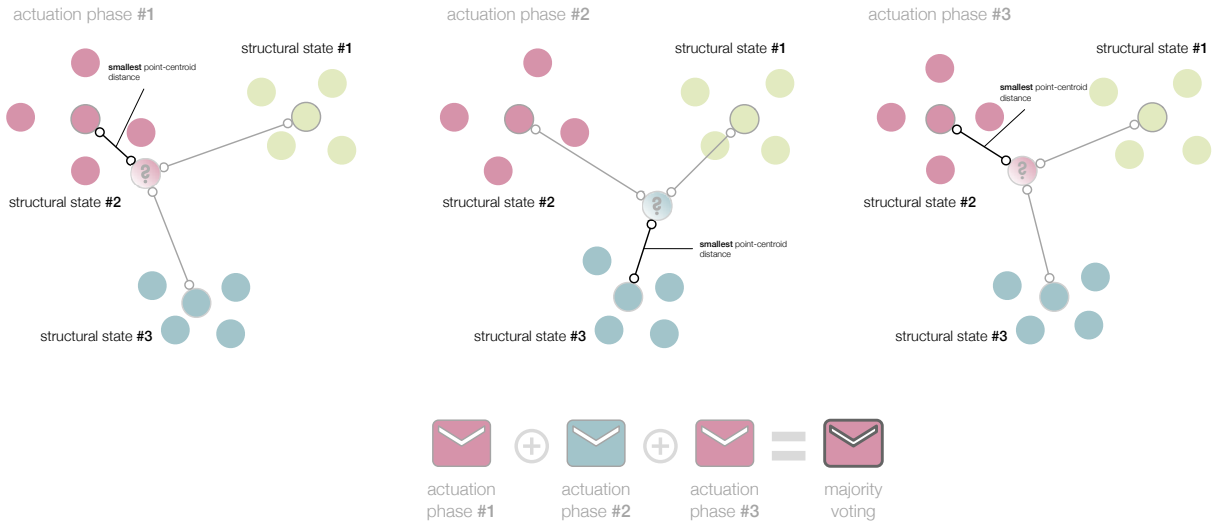

FIGURE 6 In the majority voting, the strategy of the smallest point-centroid distance is performed per actuation phase. The current structure to diagnose is associated with the most voted structural state.

5 | RESULTS

The results of damage detection and classification (introduced in Sections 2 and 3 and detailed in Sections 4.3–4.5) for the aluminum plate are presented in terms of the confusion matrices for the scenarios defined in Section 4.2. We present the results for each scenario in a different section. Specifically, Section 5.1 presents the results for **Scenario 1**. Section 5.2 and Section 5.3 present the results for **Scenario 2** and **Scenario 3**, respectively. In the three scenarios, four different structural states have been considered. The first structural state corresponds to the healthy state of the structure: the square aluminum plate with no damage (denoted as $D0$). The second, third, and fourth structural states correspond to the plate with an added mass at the positions indicated in Figures 4(a) and 4(b) (denoted as $D1$, $D2$, and $D3$, respectively).

To validate the method of damage detection and classification from Sections 4.3–4.5, we will perform five iterations ($\kappa = 5$) of a non-exhaustive leave-p-out cross-validation, where $p = 80$, as described in Section 4.4. At each iteration, we have considered 80 observations according to the following distribution: 20 observations per structural state ($D0$, $D1$, $D2$, and $D3$). Because 80 observations have been used for the validation step in $\kappa = 5$ iterations, the sum of all the elements in the confusion matrices that we will present in Sections 5.1, 5.2, and 5.3 is equal to $5 \cdot 80 = 400$.

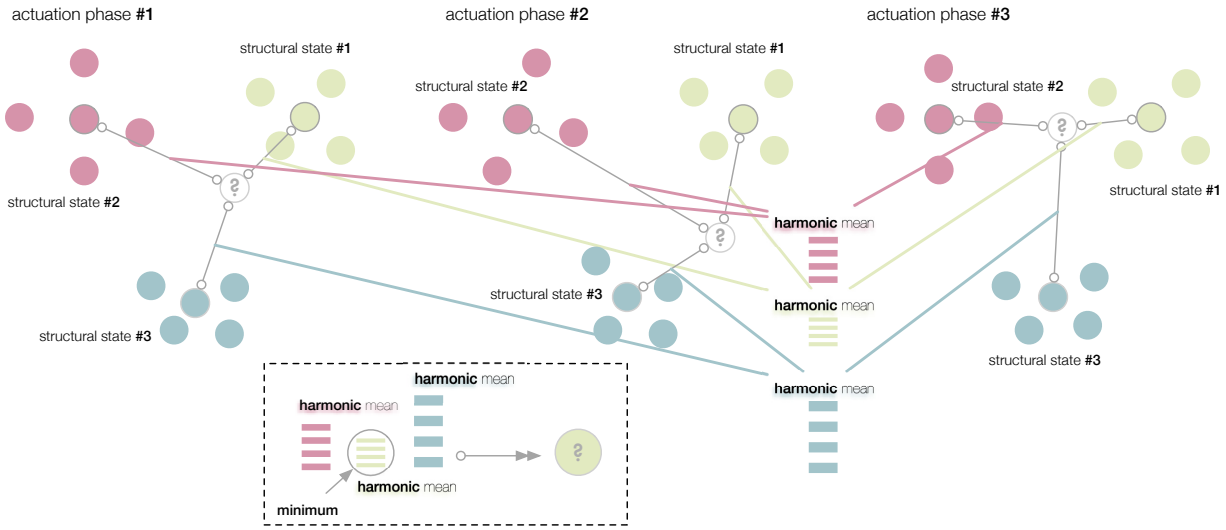

FIGURE 7 In the "sum of the inverse distances" approach, the current structure to diagnose is associated with the structural state with the minimum harmonic mean of the distances between the centroids (the points with a gray stroke) and the map point (the points with a question mark).

Hence, for the three scenarios, we present five different confusion matrices:

- **Actuation phase 1** and **Actuation phase 3**. Damage detection and classification are applied to a single matrix, $\mathbf{X}[1]$ or $\mathbf{X}[3]$, as in Equation (16), using the smallest point-centroid distance.
- **Actuation phases 1–4**. Damage detection and classification are applied to a single matrix: the horizontal concatenation of the four matrices $X[\varphi],\ \varphi = 1, \ldots, 4$, namely $\mathbf{X}[1, 2, 3, 4]$, as in Equation (17), using the smallest point-centroid distance.
- **Majority voting**. Damage detection and classification are applied to the four matrices: $X[\varphi],\ \varphi = 1, \ldots, 4$. Each actuation phase casts a vote, and a final decision is taken using the majority voting (Section 4.5).
- **Sum of the inverse distances**. Damage detection and classification are applied to the four matrices: $X[\varphi],\ \varphi = 1, \ldots, 4$. Each actuation phase casts a vote, and a final decision is taken based on the maximum sum of the inverse distances (Section 4.5).

Finally, in some cases, to compare the performance of the current approach to damage detection and classification, we have included confusion matrices of a similar approach. The approach that is used to compare the performance of *t*-SNE relies on the same strategy for data integration (Section 2.1) and data transformation (Section 2.2). The difference is that the clusters are created using PCA, instead of *t*-SNE.

5.1 | Scenario 1

In this section, we present the results for **Scenario 1**. In this scenario, a short wire has been used, and the measured signals are filtered with a Savitzky–Golay algorithm. Tables 1 and 3 show the five confusion matrices. When the decision is based on a single actuation phase (Table 1), the overall accuracy is quite good. Specifically, 396 and 397 observations out of 400 cases have been correctly classified in actuation phases 1 and 3, respectively (which corresponds to an overall accuracy of 99% and 99.25%, respectively). When the four actuation phases are used simultaneously (actuation phases 1–4, Equation (17), the majority voting and the sum of the inverse distances), we achieve an overall accuracy of 100%, as shown in Table 3.

In this scenario, which is the most advantageous, the PCA-based damage detection and classification also perform well. However, the overall accuracy is reduced to 94.5% (Table 2). This is the first indication that the clusters created with *t*-SNE have a better quality compared with the clusters created with PCA.

TABLE 1 Confusion matrix of the application of the *t*-SNE based damage detection and classification procedure presented in Sections 2 and 3 to the case of the aluminum plate (**Scenario 1**) described in Section 4.1, for the actuation phases 1 and 3.

		Actuation phase 1				**Actuation phase** 3			
True \ **Predicted**		*D*0	*D*1	*D*2	*D*3	*D*0	*D*1	*D*2	*D*3
*D*0		96	0	2	2	99	0	0	1
*D*1		0	100	0	0	0	100	0	0
*D*2		0	0	100	0	1	0	98	1
*D*3		0	0	0	100	0	0	0	100

*D*0: healthy state of the structure; *D*1, *D*2, and *D*3: added masses at the positions indicated in Figures 4(a) and 4(b).

TABLE 2 Confusion matrix of the application of the PCA-based damage detection and classification procedure to the case of the aluminum plate (**Scenario 1**) described in Section 4.1, for the actuation phases 1 and 3.

		Actuation phase 1				**Actuation phase** 3			
True \ **Predicted**		*D*0	*D*1	*D*2	*D*3	*D*0	*D*1	*D*2	*D*3
*D*0		78	0	0	22	100	0	0	0
*D*1		0	100	0	0	0	100	0	0
*D*2		0	0	100	0	2	0	78	20
*D*3		0	0	0	100	0	0	0	100

*D*0: healthy state of the structure; *D*1, *D*2, and *D*3: added masses at the positions indicated in Figures 4(a) and 4(b).

5.2 | Scenario 2

In this section, we present the results for **Scenario 2**. In this case, a short wire has been used, but the measured signals were not filtered. Tables 4 and 6 show the five confusion matrices. When the decision is based on a single actuation phase (Table 4), the overall accuracy is quite remarkable. Specifically, for actuation phase 1, 382 observations out of 400 have been correctly classified (which corresponds to an overall accuracy of 95.5%). For actuation phase 3, when the four actuation phases are used simultaneously (actuation phases 1–4, Equation (17), the majority voting and the sum of the inverse distances), an overall accuracy of 100% is achieved, as shown in Table 6.

Moreover, in this case, the results of the *t*-SNE based damage detection and classification are compared to those of the PCA-based method. In particular, in actuation phase 1, 289 observations out of 400 have been correctly classified (Table 5). This corresponds to an overall accuracy of 72.25%. The *t*-SNE based damage detection and classification (with an overall accuracy of 95.5%) outperforms the PCA-based approach. Moreover, the false-positive rate (FPR)—defined as the ratio of false positives to the total number of negatives—is $49/100 = 49\%$, which is unsatisfactory. Similarly, the false-negative rate (FNR)—the ratio of false negatives to the total number of positives—is $34/300 = 11.3\%$. To compute the FNR, the three different types of damage (*D*1, *D*2, and *D*3) are considered as a single category (the opposite of the healthy state of the structure).

TABLE 3 Confusion matrix of the application of the *t*-SNE based damage detection and classification procedure presented in Sections 2 and 3 to the case of the aluminum plate (**Scenario 1**) described in Section 4.1, when the four actuation phases are used simultaneously.

True \ Predicted	Phases 1–4				Majority voting				Inverse distances			
	*D*0	*D*1	*D*2	*D*3	*D*0	*D*1	*D*2	*D*3	*D*0	*D*1	*D*2	*D*3
*D*0	100	0	0	0	100	0	0	0	100	0	0	0
*D*1	0	100	0	0	0	100	0	0	0	100	0	0
*D*2	0	0	100	0	0	0	100	0	0	0	100	0
*D*3	0	0	0	100	0	0	0	100	0	0	0	100

*D*0: healthy state of the structure; *D*1, *D*2, and *D*3: added masses at the positions indicated in Figures 4(a) and 4(b).

TABLE 4 Confusion matrix of the application of the *t*-SNE based damage detection and classification procedure presented in Sections 2 and 3 to the case of the aluminum plate (**Scenario 2**) described in Section 4.1, for the actuation phases 1 and 3.

True \ Predicted	Actuation phase 1				Actuation phase 3			
	*D*0	*D*1	*D*2	*D*3	*D*0	*D*1	*D*2	*D*3
*D*0	82	6	12	0	100	0	0	0
*D*1	0	100	0	0	0	100	0	0
*D*2	0	0	100	0	0	0	100	0
*D*3	0	0	0	100	0	0	0	100

*D*0: healthy state of the structure; *D*1, *D*2, and *D*3: added masses at the positions indicated in Figures 4(a) and 4(b).

5.3 | Scenario 3

In this section, we present the results for **Scenario 3**. In the two previous scenarios, a short wire was used. However, in this case, the signals are acquired using a 2.5 m long wire. Tables 7 and 8 show the five confusion matrices. When the decision is based on a single actuation phase (Table 7), the overall accuracy significantly decreases compared with **Scenario 1** and **Scenario 2**. Specifically, 244 and 280 observations have been correctly classified in the actuation phases 1 and 3, respectively (which represents an overall accuracy of 61% and 70%, respectively). For actuation phase 1, the FPR is 50%, and the FNR is 16%: both values are unacceptable.

The potential of the approaches where the four actuation phases are used can be observed in this last scenario (see Table 8):

- When the four actuation phases are merged in a single matrix (as in Equation (17)), 354 observations out of 400 are correctly classified; this represents an overall accuracy of 88.5%, an FPR of 14%, and an FNR of 4%.
- When each actuation phase casts a vote, and a final decision is taken using the majority voting, the overall accuracy is increased to 91.25%. The FPR is reduced to 2%, and the FNR is slightly increased to 6%.
- Finally, when each actuation phase casts a vote, and a final decision is taken using the maximum sum of the inverse distances, the overall accuracy increases to 97%. FPR and FNR are significantly reduced to 1% and 1%, respectively.

Table 9 summarizes the values for the overall accuracy, FPR, and FNR in this scenario.

TABLE 5 Confusion matrix of the application of the PCA-based damage detection and classification procedure to the case of the aluminum plate (**Scenario 2**) described in Section 4.1, for the actuation phases 1 and 3.

	Actuation phase 1				**Actuation phase** 3			
Predicted / **True**	*D*0	*D*1	*D*2	*D*3	*D*0	*D*1	*D*2	*D*3
*D*0	51	8	40	1	100	0	0	0
*D*1	4	76	20	0	0	100	0	0
*D*2	26	2	70	2	0	0	100	0
*D*3	4	0	4	92	0	0	0	100

*D*0: healthy state of the structure; *D*1, *D*2, and *D*3: added masses at the positions indicated in Figures 4(a) and 4(b).

TABLE 6 Confusion matrix of the application of the *t*-SNE based damage detection and classification procedure presented in Sections 2 and 3 to the case of the aluminum plate (**Scenario 2**) described in Section 4.1, when the four actuation phases are used simultaneously.

	Phases 1–4				**Majority voting**				**Inverse distances**			
Predicted / **True**	*D*0	*D*1	*D*2	*D*3	*D*0	*D*1	*D*2	*D*3	*D*0	*D*1	*D*2	*D*3
*D*0	100	0	0	0	100	0	0	0	100	0	0	0
*D*1	0	100	0	0	0	100	0	0	0	100	0	0
*D*2	0	0	100	0	0	0	100	0	0	0	100	0
*D*3	0	0	0	100	0	0	0	100	0	0	0	100

*D*0: healthy state of the structure; *D*1, *D*2, and *D*3: added masses at the positions indicated in Figures 4(a) and 4(b).

TABLE 7 Confusion matrix of the application of the *t*-SNE based damage detection and classification procedure presented in Sections 2 and 3 to the case of the aluminum plate (**Scenario 3**) described in Section 4.1, for the actuation phases 1 and 3.

	Actuation phase 1				**Actuation phase** 3			
Predicted / **True**	*D*0	*D*1	*D*2	*D*3	*D*0	*D*1	*D*2	*D*3
*D*0	50	6	19	25	93	1	3	3
*D*1	19	66	11	4	16	50	23	11
*D*2	14	3	73	10	5	19	70	6
*D*3	15	9	21	55	0	23	10	67

*D*0: healthy state of the structure; *D*1, *D*2, and *D*3: added masses at the positions indicated in Figures 4(a) and 4(b).

5.4 | General comments

According to the results presented in Sections 5.1–5.3, it is better to make a decision considering all of the actuation phases (assembling these phases or using them to cast a vote) rather than working with the phases separately. Moreover, the results

reveal the strong performance of the "sum of the inverse distances" strategy as compared to the majority voting or the horizontal concatenation of the four actuation phases. The majority voting outperforms the horizontal concatenation of the four actuation phases, but it cannot accurately classify damage $D1$ (**Scenario 3**, Table 8). In contrast, the "sum of the inverse distances" strategy classifies the practical totality of the kinds of damage that we have considered. In general, the healthy state of the structure is confused with a damaged structure only in a few cases. Similarly, the damaged structure is identified as a structure with no damage in a very limited number of observations. In general, the performance of the proposed method is satisfactory when the signals are acquired using a short wire, with or without adding white Gaussian noise. In these two cases, if using PCA as a preprocessing step, the noise is canceled. The third scenario presents the worst case, because it used a long cable (2.5 m) from the digitizers to the sensors. In this scenario, the signals were badly digitized (because of the impedance of the cable, the low voltage of the stimulus, and other experimental characteristics). Therefore, we observe that the use of a long cable from the digitizer to the sensors affects the quality of detection and classification. However, combining the four actuation phases and the "sum of the inverse distances" strategy, we can obtain very accurate results.

TABLE 8 Confusion matrix of the application of the t-SNE based damage detection and classification procedure presented in Sections 2 and 3 to the case of the aluminum plate (**Scenario 3**) described in Section 4.1, when the four actuation phases are used simultaneously.

		Phases 1–4				**Majority voting**				**Inverse distances**			
True \ **Predicted**		$D0$	$D1$	$D2$	$D3$	$D0$	$D1$	$D2$	$D3$	$D0$	$D1$	$D2$	$D3$
$D0$		86	1	7	6	98	0	0	2	99	0	1	0
$D1$		8	88	4	0	12	85	2	1	1	99	0	0
$D2$		1	8	89	2	6	2	90	2	1	1	95	3
$D3$		3	4	2	91	0	3	5	92	1	2	2	95

$D0$: healthy state of the structure; $D1$, $D2$, and $D3$: added masses at the positions indicated in Figures 4(a) and 4(b).

TABLE 9 Overall accuracy, FPR, and FNR of the application of the t-SNE based damage detection and classification procedure presented in Sections 2 and 3 to the case of the aluminum plate (**Scenario 3**) described in Section 4.1, when the four actuation phases are used separately and simultaneously.

	Accuracy	FPR	FNR
Actuation phase 1	61.0%	50.0%	16.0%
Actuation phase 3	70.0%	7.0%	7.0%
Phases 1-4	88.5%	14.0%	4.0%
Majority voting	91.3%	2.0%	6.0%
Inverse distances	97.0%	1.0%	1.0%

6 | CONCLUSIONS

In this study, we proposed an SHM strategy for detection and classification of structural changes using two-step data integration (type *E* unfolding and MCGS), data transformation using PCA, and two-step data reduction combining PCA and *t*-SNE. We evaluated the proposed approach using experimental data. In general, the obtained results show that the performance of the proposed method is very satisfactory, given its high classification accuracy. The performance is very good and similar in all the datasets. In the case studies, we obtain very accurate results regardless of adding white Gaussian noise, because PCA cancels the noise. However, the use of a long wire (2.5 m) from the digitizers to the sensors reduces the quality of detection and classification. Moreover, we can obtain accurate results by combining the four actuation phases and the "sum of the inverse distances" strategy. Results also show that the quality of the 2-dimensional clusters created with *t*-SNE is better than the quality of the equivalent 2-dimensional clusters created only with PCA; thus, *t*-SNE improves the classification. Therefore, the *t*-SNE based damage detection and classification significantly outperforms the PCA-only-based approach. Some aspects to highlight in the proposed method are as follows. First, the *t*-SNE technique has been extended and adapted to the field of SHM to detect and classify structural changes. Second, our method classifies the current state of the structure using data-driven analysis (that is, using the data collected from the structure under different structural states) and without the use of complex mathematical models. Third, our results show that it is better to make a decision considering all of the actuation phases (assembling these phases or using them to cast a vote) rather than working with the phases separately. Fourth, our findings show the strong performance of the "sum of the inverse distances" strategy compared with the majority voting or the horizontal concatenation of the four actuation phases. Fifth, the majority voting outperforms the horizontal concatenation of the four actuation phases. Finally, in general, the healthy state of the structure is confused with a damaged structure only in a few cases; similarly, a damaged structure is identified as a structure with no damage in a very limited number of observations. Regarding the possible fields of application, similar aluminum plates have been used to represent parts of a plane (wings or fuselage). We think that we can also apply this approach to detect damage and faults in wind turbines. In general, there is no prescribed field of application: if a sensor network can be installed in a structure, and several actuation phases can be considered, the proposed approach can be *a priori* implemented. In future work, we plan to apply the proposed method to different EOC to determine its effectiveness, as well as to handle imbalanced data. Besides, we aim to investigate the parametric version of *t*-SNE.

ACKNOWLEDGEMENTS

This work has been partially funded by the Spanish Agencia Estatal de Investigación (AEI), Ministerio de Economía, Industria y Competitividad (MINECO), by the Fondo Europeo de Desarrollo Regional (FEDER) through the research project DPI2017-82930-C2-1-R, and by the Generalitat de Catalunya through the research project 2017 SGR 388. We gratefully acknowledge the support of NVIDIA Corporation that donated the Titan Xp GPU used for this research. We thank the Universitat Politècnica de Catalunya (UPC) for the predoctoral fellowship to D. Agis.

References

1. Raju KS, Pratap Y, Sahni Y, Babu MN. Implementation of a WSN system towards SHM of civil building structures. In: *2015 IEEE 9th International Conference on Intelligent Systems and Control (ISCO)*; 2015: 1–7.
2. Blanco H, Boffill Y, Lombillo I, Villegas L. An integrated structural health monitoring system for determining local/global responses of historic masonry buildings. *Structural Control and Health Monitoring* 2018; 25(8): e2196.
3. Ciang CC, Lee JR, Bang HJ. Structural health monitoring for a wind turbine system: a review of damage detection methods. *Measurement Science and Technology* 2008; 19(12): 122001.
4. Loh CH, Loh KJ, Yang YS, Hsiung WY, Huang YT. Vibration-based system identification of wind turbine system. *Structural Control and Health Monitoring* 2017; 24(3): e1876.
5. Nisha M. Structural health monitoring of aircraft wing using wireless network. *International Journal of Technological Exploration and Learning* 2014; 3(1): 341–343.
6. Ochôa P, Groves RM, Benedictus R. Systematic multiparameter design methodology for an ultrasonic health monitoring system for full-scale composite aircraft primary structures. *Structural Control and Health Monitoring* 2019; 26: e2340.
7. Ward MO, Grinstein G, Keim D. *Interactive data visualization: foundations, techniques, and applications*. Boca Raton, FL, USA: CRC Press . 2015.

8. Tenenbaum JB, De Silva V, Langford JC. A global geometric framework for nonlinear dimensionality reduction. *Science* 2000; 290(5500): 2319–2323.

9. van der Maaten L, Hinton G. Visualizing data using t-SNE. *Journal of Machine Learning Research* 2008; 9(Nov): 2579–2605.

10. Westerhuis JA, Kourti T, MacGregor JF. Comparing alternative approaches for multivariate statistical analysis of batch process data. *Journal of Chemometrics: A Journal of the Chemometrics Society* 1999; 13(3-4): 397–413.

11. Mujica L, Rodellar J, Fernandez A, Güemes A. Q-statistic and T2-statistic PCA-based measures for damage assessment in structures. *Structural Health Monitoring* 2011; 10(5): 539–553.

12. Vidal Y, Pozo F, Tutivén C. Wind turbine multi-fault detection and classification based on SCADA data. *Energies* 2018; 11(11): 3018.

13. Sikdar S, Kundu A, Jurek M, Ostachowicz W. Nondestructive analysis of debonds in a composite structure under variable temperature conditions. *Sensors* 2019; 19(16): 3454.

14. Yan J, Jin H, Sun H, Qing X. Active monitoring of fatigue crack in the weld zone of bogie frames using ultrasonic guided waves. *Sensors* 2019; 19(15): 3372.

15. Cho H, Hasanian M, Shan S, Lissenden CJ. Nonlinear guided wave technique for localized damage detection in plates with surface-bonded sensors to receive Lamb waves generated by shear-horizontal wave mixing. *NDT & E International* 2019; 102: 35–46.

16. Jiménez AA, Muñoz CQG, Márquez FPG. Dirt and mud detection and diagnosis on a wind turbine blade employing guided waves and supervised learning classifiers. *Reliability Engineering & System Safety* 2019; 184: 2–12.

17. Pozo F, Vidal Y, Salgado Ó. Wind turbine condition monitoring strategy through multiway PCA and multivariate inference. *Energies* 2018; 11(4): 749.

18. Hinton G, Roweis ST. Stochastic neighbor embedding. In: *Advances in Neural Information Processing Systems*; 2003: 857–864.

19. Min R. *A non-linear dimensionality reduction method for improving nearest neighbour classification*. PhD thesis. University of Toronto, 2005.

20. Orfanidis SJ. *Introduction to signal processing*. Upper Saddle River, NJ, USA: Prentice-Hall, Inc. . 1995.

21. Vitola J, Pozo F, Tibaduiza DA, Anaya M. A sensor data fusion system based on *k*-nearest neighbor pattern classification for structural health monitoring applications. *Sensors* 2017; 17(2): 417.

22. Vitola J, Pozo F, Tibaduiza DA, Anaya M. Distributed piezoelectric sensor system for damage identification in structures subjected to temperature changes. *Sensors* 2017; 17(6): 1252.

23. Tardy B, Inglada J, Michel J. Assessment of optimal transport for operational land-cover mapping using high-resolution satellite images time series without reference data of the mapping period. *Remote Sensing* 2019; 11(9): 1047.

24. Mehta S, Shen X, Gou J, Niu D. A new nearest centroid neighbor classifier based on *k* local means using harmonic mean distance. *Information* 2018; 9(9): 234.

How to cite this article: Agis, D., Tibaduiza, D.A., and Pozo, F. (2019), Vibration-based detection and classification of structural changes using principal component analysis and *t*-distributed stochastic neighbor embedding, *Structural Control and Health Monitoring*, *2020;00:1–6*.